Nonlinear Camera Response Functions and Image Deblurring: Theoretical Analysis and Practice

Yu-Wing Tai[1] Xiaogang Chen[2,5] Sunyeong Kim[1] Seon Joo Kim[3] Feng Li[4]
Jie Yang[2] Jingyi Yu[5] Yasuyuki Matsushita[6] Michael S. Brown[7]
[1]KAIST, [2]Shanghai Jiao Tong University, [3]Yonsei University, [4]MERL,
[5]University of Delaware, [6]MSRA, [7]National University of Singapore

***Abstract*— This paper investigates the role that nonlinear camera response functions (CRFs) have on image deblurring. We present a comprehensive study to analyze the effects of CRFs on motion deblurring. In particular, we show how nonlinear CRFs can cause a spatially invariant blur to behave as a spatially varying blur. We prove that such nonlinearity can cause large errors around edges when directly applying deconvolution to a motion blurred image without CRF correction. These errors are inevitable even with a known point spread function (PSF) and with state-of-the-art regularization based deconvolution algorithms. In addition, we show how CRFs can adversely affect PSF estimation algorithms in the case of blind deconvolution. To help counter these effects, we introduce two methods to estimate the CRF directly from one or more blurred images when the PSF is known or unknown. Our experimental results on synthetic and real images validate our analysis and demonstrate the robustness and accuracy of our approaches.**

***Index Terms*— Nonlinear Camera Response Functions (CRFs), Motion Deblurring, CRF Estimation**

I. Introduction

Image deblurring is a long standing computer vision problem for which the goal is to recover a sharp image from a blurred image. Mathematically, the problem is formulated as:

$$B = I \otimes K + n, \tag{1}$$

where B is the captured blurred image, I is the latent image, K is the point spread function (PSF), $\otimes$ is the convolution operator, and n represents image noise.

One common assumption in most previous algorithms that is often overlooked is that the image B in Equation (1) responds in a linear fashion with respect to irradiance, *i.e.*, the final image intensity is proportional to the amount of light received by the sensor. This assumption is valid when we capture an image in a RAW format. However, when capturing an image using a common consumer level camera or camera on a mobile device, there is a nonlinear camera response function(CRF) that maps the scene irradiance to intensity. CRFs vary among different camera manufacturers and models due to design factors such as compressing the scene's dynamic range or to simulate conventional irradiance responses of film [15], [33]. Taking this nonlinear response into account, the imaging process of Equation (1) can be considered as:

$$B = f(I \otimes K + n), \tag{2}$$

where $f(\cdot)$ is the CRF. To remove the effect of the nonlinear CRF from image deblurring, the image B has to be first linearized by the inverse CRF, *i.e.*, f^{-1}. After deconvolution, the CRF is applied again to restore the original intensity which leads to the following process:

$$I = f(f^{-1}(B) \otimes K^{-1}), \tag{3}$$

where K^{-1} is inverse filter which denotes the deconvolution process.

Contributions This paper offers two contributions with regards to CRFs and their role in image deblurring. First, we provide a systematic analysis of the effect that a CRF has on the blurring process and show how a nonlinear CRF can make a spatially invariant blur behave as a spatially varying blur around edges. We prove that such nonlinearity can cause abrupt ringing artifacts around edges which are non-uniform. In addition, these artifacts are difficult to eliminated by regularization. Our analysis also shows that PSF estimation for various blind deconvolution algorithms are adversely affected by the nonlinear CRF.

Along with the theoretical analysis, we further introduce two algorithms to estimate the CRF from one or more images: the first method is based on a least-square formation when the PSF is known; the second method is formulated as a rank minimization problem when the PSF is unknown. Both of these approaches exploit the relationship between the blur profile about edges in a linearized image and the PSF. While our estimation methods cannot compete with well-defined radiometric calibration methods based on calibration patterns or multiple exposures, they are useful to produce a sufficiently accurate CRF for improving deblurring results.

Shorter versions of this work appeared in [22], [7]. This paper unifies these two concurrent independent works with more in-depth discussion and analysis of the role of CRF in deblurring, and additional experiments. In addition, a new section that analyzes the effectiveness of gamma curve correction in traditional deblurring methods, and the limitations of the proposed algorithms are presented in Section VII-A.

The remainder of our paper is organized as follow: In Section II, we review related works in motion deblurring and CRF estimation. Our theoretical analysis about the blur inconsistency introduced by a nonlinear CRF is presented in Section III, followed by the analysis on the deconvolution artifacts and PSF estimation errors in Section IV. Our two algorithms which estimate the nonlinear CRF from motion blurred image(s) with known and unknown PSF are presented in Section V. In Section VI, we present our experimental results. Section VII-A provides additional discussion about the effectiveness of gamma curve correction. Finally, we conclude our work in Section VIII.

II. Related work

Image deblurring is a classic problem with well-studied approaches including Richardson-Lucy [35], [40] and Wiener deconvolution [48]. Recently, several different directions were introduced to enhance the performance of deblurring. These include methods that use image statistics [14], [29], [18], [6], sparsity or sharp edge prediction [30], [20], [8], [2], [50], [26], [45], multiple images or hybrid imaging systems [1], [39], [9], [51], [5], [42], [43], and new blur models that account for camera motion [44], [46], [47], [19], [17]. The vast majority of these methods, however, do not consider the nonlinearity in the imaging process due to CRFs.

The goal of radiometric calibration is to compute a CRF from a given set of images or a single image. The most accurate radiometric calibration algorithms use multiple images with different exposures [12], [4], [37], [13], [15], [21], [24], [34], [28]. Our work is more related to single-image based radiometric calibration techniques [32], [33], [38], [36], [49]. In [32], the CRF is computed by observing the color distributions of local edge regions: the CRF is computed as the mapping that transforms nonlinear distributions of edge colors into linear distributions. This idea is further extended to deal with a single gray-scale image using histograms of edge regions in [33]. In [49], a CRF is estimated by temporally mixing of a step edge within a single camera exposure by the linear motion blur of a calibration pattern. Unlike [49], however, our method deals with uncontrolled blurred images.

To the best of our knowledge, there are only a handful of previous works that consider CRFs in the context of image deblurring. Examples include the work by Fergus *et al.* [14], where images are first linearized by an inverse gamma-correction with $\gamma = 2.2$. Real world CRFs, however, are often drastically different from gamma curves [15], [31]. Another example by Lu *et al.* [34] involves reconstructing a high dynamic range image from a set of differently exposed and possibly motion blurred images. Work by Cho *et al.* [10] discussed nonlinear CRFs as a cause for artifacts in deblurring, but provided little insight into why such artifacts arise. Their work suggested to avoid this by using a pre-calibrated CRF or the camera's RAW output. While a pre-calibrated CRF is undoubtedly the optimal solution, the CRF may not always be available. Moreover, work by Chakrabarti *et al.* [3] suggests that a CRF may be scene dependent when the camera is in " auto mode". Furthermore, work by Kim *et al.* [23] showed that the CRF for a given camera may vary for different camera picture styles (*e.g.*, landscape, portrait, etc).

Our work aims to provide more insight into the effect that CRFs have on the image deblurring process. In addition, we seek to provide a method to estimate a CRF from a blurred input image in the face of a missing or unreliable pre-calibrated CRF.

III. Blur inconsistency due to nonlinear CRF

We first study the role of the CRF in the image blurring process. We denote by f as the nonlinear CRF, f^{-1} as the inverse of f, I as the blur-free intensity image, $\tilde{I}$ as the irradiance image of I, *i.e.*, $I = f(\tilde{I})$, B as the observed motion blurred image with $B = f(\tilde{I} \otimes K + n)$. To focus our analysis, we follow previous work by assuming that the PSF is spatially invariant and the image noise is negligible (*i.e.*, $n \approx 0$).

We analyze the blur inconsistency introduced by a nonlinear CRF by measuring:

$$\Gamma = B - \widehat{B} \tag{4}$$

where $\widehat{B} = I \otimes K$ which denotes the conventional intensity based blurring process. Note that I is used instead of $\tilde{I}$ in $\widehat{B}$. Our goal in here is to understand where the intensity based convolution model would introduce errors when CRF correction is excluded.

Claim 1. *In uniform intensity regions,* $\Gamma = 0$.

Proof: Since pixels within the blur kernel region have uniform intensity, we have $f^{-1}(I) \otimes K = f^{-1}(I) = f^{-1}(I \otimes K)$. Therefore,

$$B = f(f^{-1}(I) \otimes K) = f(f^{-1}(I \otimes K)) = \widehat{B}, \tag{5}$$

thus $\Gamma = 0$. ■

Claim 1 applies to any CRF (both linear or nonlinear). This implies that a nonlinear CRF will not affect deblurring quality for uniform intensity regions.

Claim 2. *If the blur kernel K is small and the CRF f is smooth,* $\Gamma \approx 0$ *in low frequency regions* .

Proof: Let $I = \overline{I} + \Delta I$ be a local patch covered by the blur kernel K. The term $\overline{I}$ is the average intensity within the patch and ΔI is the deviation from $\overline{I}$. In low frequency regions, ΔI is small.

Next, we apply the first-order Taylor series expansion to $f^{-1}(I) \otimes K$ as:

$$f^{-1}(\overline{I} + \Delta I) \otimes K \approx f^{-1}(\overline{I}) \otimes K + (f'^{-1}(\overline{I}) \cdot \Delta I) \otimes K, \tag{6}$$

where f'^{-1} is the first order derivative of f^{-1}. Since $\overline{I}$ is uniform, we have $f^{-1}(\overline{I}) \otimes K = f^{-1}(\overline{I})$ and $f'^{-1}(\overline{I})$ is constant in the local neighborhood. Thus, Equation (6) can be approximated as:

$$f^{-1}(\overline{I}) + f'^{-1}(\overline{I}) \cdot \Delta I \otimes K. \tag{7}$$

Similarly, by using the first-order Taylor series expansion, we have

$$\begin{aligned} f^{-1}(I \otimes K) &= f^{-1}(\overline{I} \otimes K + \Delta I \otimes K) \\ &\approx f^{-1}(\overline{I} \otimes K) + f'^{-1}(\overline{I} \otimes K) \cdot (\Delta I \otimes K) \quad (8) \\ &= f^{-1}(\overline{I}) + f'^{-1}(\overline{I}) \cdot \Delta I \otimes K. \quad (9) \end{aligned}$$

Therefore,

$$B = f(f^{-1}(I) \otimes K) \approx f(f^{-1}(I \otimes K)) = \widehat{B}, \tag{10}$$

i.e., $\Gamma \approx 0$. ■

Claim 2 holds only for small kernels. When the kernel size is large, *e.g.*80×80, the first-order Taylor series expansion is not accurate. To illustrate this property, we simulate a 1D smooth signal in Figure 1(a). A uniform motion blur kernel with different size (10, 20, 30 and 80 pixels) is applied to the 1D signal. We compute B and $\widehat{B}$ with f^{-1} being a gamma curve ($\gamma = 2.2$). The plotting of Γ along the 1D signal with different sized Ks are shown in Figure 1(a). Note that $\Gamma \approx 0$ for the first three kernels.

Claim 3. Γ *can be large at high frequency high contrast regions.*

Proof: Let us consider a sharp edge in I represented by a Step Edge Function,

$$I(x) = \begin{cases} 0, & \text{if } x < 0.5 \\ 1, & \text{otherwise} \end{cases} \tag{11}$$

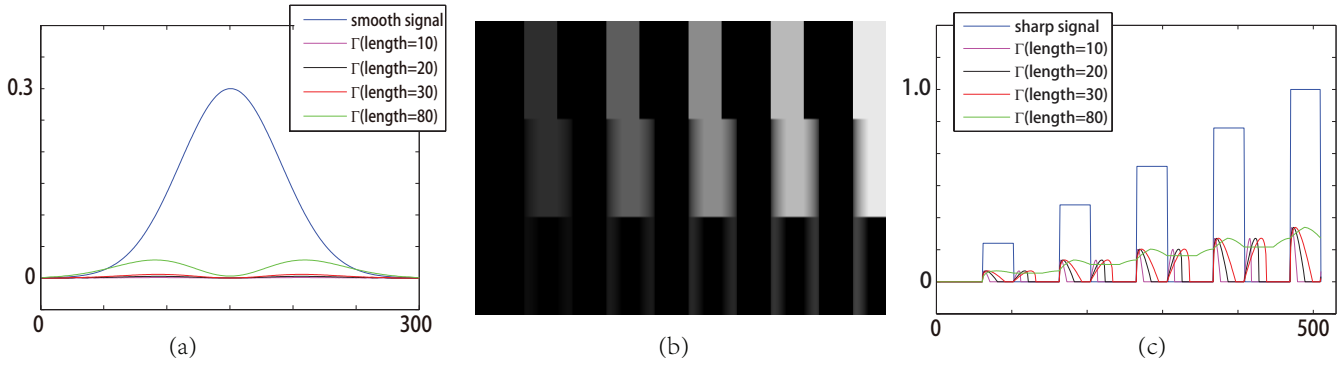

Fig. 1. Illustration of blur inconsistency Γ. A gamma curve with $\gamma = 2.2$ is used to simulate f^{-1} across all sub-figures. (a): Γ is computed along a 1D smooth signal with four different uniform motion blur kernels of size 10, 20, 30 and 80 pixels. (b) The first two rows show the latent pattern and the corresponding irradiance-based motion blurred pattern respectively. The bottom row shows the measured Γ which varies across different edge strength. (c) Plotting of Γ in (b) with different kernel sizes.

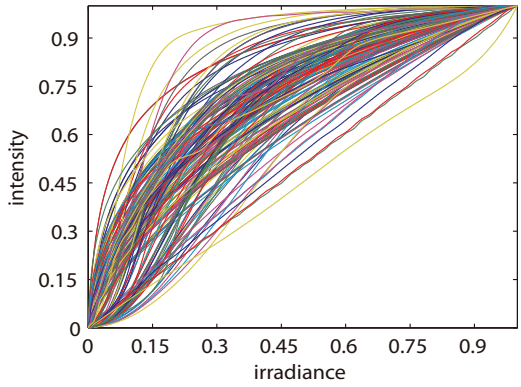

Fig. 2. The left panel shows 188 CRF curves of real cameras from DoRF [15]. Nearly all curves appear concave.

Since f^{-1} has boundary $f^{-1}(0) = 0$ and $f^{-1}(1) = 1$ [15], we have $f^{-1}(I) = I$. Therefore,

$$B = f(f^{-1}(I) \otimes K) = f(I \otimes K) = f(\widehat{B}), \tag{12}$$

Hence, $\Gamma = f(\widehat{B}) - \widehat{B}$. ■

In this example, $\Gamma(x)$ measures how $f(x)$ deviates from the linear function $y(x) = x$. In other words, $\Gamma(x) \to 0$, *iff* $f(x) \to x$. However, practical CRFs f are highly nonlinear [15], [23].

To validate Claim 3, we simulate a 1D signal of sharp edges with different gradient magnitudes and measure the blur inconsistency Γ as shown in Figure 1(b). The first row is the original clear signal. The second row is the blur signal B where the blur kernel size is 20 pixels. The third row shows the Γ which is non-zero around edge regions and the Γ increase as the gradient magnitudes get larger. To further analyze the effect of kernel size on sharp signals, we plot Γ with four different sized kernels in Figure 1(c). Notice that the area of non-zero Γ increase with kernel size since the blurry edge gets larger. Also, the magnitude of Γ depends on edge magnitude but it does not depends on kernel size.

Theorem 1. *Let I_{min} and I_{max} be the local minimum and maximum pixel intensities in a local neighborhood covered by kernel K in image I. If f^{-1} is convex, then the Blur Inconsistency is bounded by $0 \leq \Gamma \leq I_{max} - I_{min}$.*

Proof: Consider $f^{-1}(I) \otimes K$ as a convex combination of pixels from $f^{-1}(I)$ since K contains only zero or positive values. If f^{-1} is convex, we can use the Jensen's inequality to obtain

$$f^{-1}(I) \otimes K \geq f^{-1}(I \otimes K). \tag{13}$$

Further, since the CRF f is a monotonically increasing [12], [37], we have:

$$B = f(f^{-1}(I) \otimes K) \geq f(f^{-1}(I \otimes K)) = \widehat{B}, \tag{14}$$

i.e., $\Gamma \geq 0$.

Next, we derive the upper bound of Γ. Since $I \otimes K \leq I_{max}$ and f^{-1} is monotonically increasing (as f^{-1} is inverse of f and f is monotonically increasing), $f^{-1}(I) \otimes K \leq f^{-1}(I_{max})$. Therefore, we have,

$$B = f(f^{-1}(I) \otimes K) \leq f(f^{-1}(I_{max})) = I_{max}. \tag{15}$$

Likewise, we can also derive $\widehat{B} = I \otimes K \geq I_{min}$. Combining this with Equation (14) and Equation (15), we have: $I_{min} \leq \widehat{B} \leq B \leq I_{max}$. Therefore,

$$0 \leq \Gamma \leq I_{max} - \widehat{B} \leq I_{max} - I_{min}. \tag{16}$$

■

Theorem 1 explains the phenomenon in Figure 1: when the gradient magnitude of an edge is large, the upper-bound of Γ will be large. On the other hand, in low contrast regions, the upper bound $I_{max} - I_{min}$ is small and so is Γ. Thus, B can be well approximated by $\widehat{B}$.

It is important to note that Theorem 1 assumes a convex inverse CRF f^{-1}. This property has been observed in many previous results. For example, the widely used Gamma curves $f^{-1}(x) = x^{\gamma}, \gamma > 1$, are convex. To better illustrate the convexity of f^{-1} (or equally the concavity of f), we plot 188 real camera CRF curves (f) collected in [15] in Figure 2. We compute the discrete second-order derivatives of the 188 real camera CRF curves. Our experiment shows that the majority (84.4%) of sample points are negative and therefore the inverse CRF f^{-1} is largely convex.

Combining Claim 1, 2, 3, and theory 1, we see that the blur inconsistency introduced by nonlinear CRF mainly appears in high contrast high frequency regions in original signal. These regions, however, are the regions that mostly cause ringing artifacts in image deblurring. Next, we will analysis the effects of CRF and how it affects the quality of image deblurring.

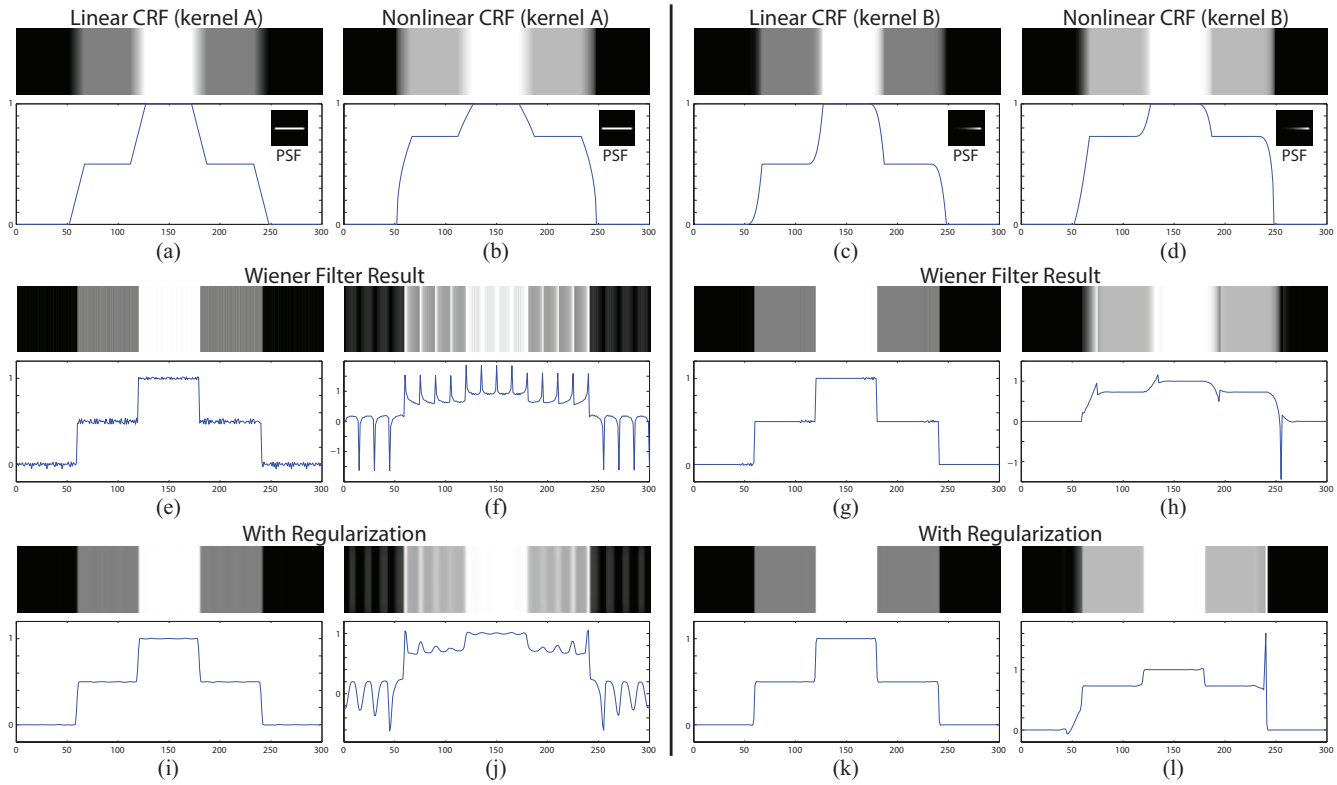

Fig. 3. This figure shows a simple step edge image that has been blurred by two different PSF kernels: a 1D motion PSF with uniform speed (kernel A) and a 1D PSF with non-uniform speed (kernel B). These blurred images are transformed with a linear CRF (a)(c), and with a nonlinear CRF (b)(d). The 1D PSF and the 1D slice of intensity values are also shown. (e)-(h) show non-blind deconvolution results of (a)-(d) using Wiener filter. (i)-(l) show non-blind deconvolution results of (a)-(d) using an iterative re-weighting method [30] with sparsity regularization.

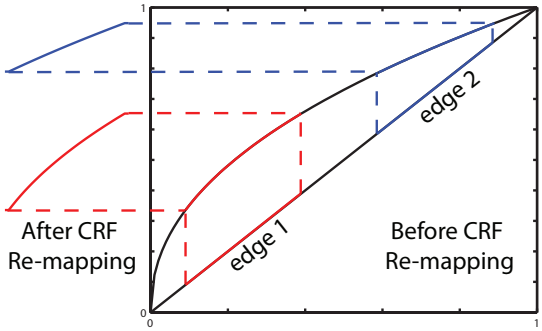

Fig. 4. This figure illustrates the problem when the image intensities are re-mapped according to different part of the camera response function. Two identical edge profiles at different intensity ranges are re-mapped to have different shapes.

IV. Effects of CRF in Image Deblurring

A. Effects on PSF and image deconvolution

We begin our analysis using synthetic examples shown in Figure 3. An image with three different intensity levels (Black, Gray, and White) is blurred with 1D motion PSFs with uniform speed (kernel A) and non-uniform speed (kernel B) to generate the observations in Figure 3 (a)(b) and Figure 3 (c)(d) respectively. A real CRF [1] is used to nonlinearly re-map the image intensity in Figure 3 (b)(d) after convolution.

In this example, we can observe how the blur profiles of an image becomes spatially varying after the nonlinear re-mapping of image intensities even though the underlying motion PSF is spatially invariant. With a linear CRF, the blur profile from the black to gray region (first step edge) is the same as the blur profile from the gray to white region (second step edge) as shown in Figure 3 (a)(c). However, with a nonlinear CRF, the two blur profiles become different as shown in Figure 3 (b)(d). This is because the slope and the curvature of the CRF are different for different range of intensities. Figure 4 helps to illustrate this effect.

To examine the effect that these cases have on image deblurring, we performed non-blind deconvolution on the synthetic images as shown in the second and third rows of Figure 3. The second row shows the results of Wiener filtering [48] while the third row shows the results of [30] with sparsity regularization. Without using any regularization, the deblurring results of both the linear and nonlinear CRF contain ringing artifacts due to the zero component of the PSF in the frequency domain. However, the magnitude of these ringing artifacts in the nonlinear CRF result is significantly larger than the one with the linear CRF. The use of image regularization [30] helps to reduce the ringing artifacts, but the regularization is less effective in the case of a nonlinear CRF even with a very large regularization weight.

In addition, if we assume I is a step edge and f is a Gamma function, $f(x) = x^{\gamma}$ with $\gamma < 1$, we can re-write $B = f(\widehat{B})$ (Equation (12)) using Taylor series expansion:

$$B = \widehat{B}^{\gamma} = \widehat{B} + P, \tag{17}$$

where $P = \sum_{\kappa=1}^{\infty} \frac{(\gamma-1)^{\kappa}}{\kappa!} \widehat{B}(\ln \widehat{B})^{\kappa}$. An important property of function $x(\ln x)^{\kappa}$ is that it approaches zero for $x \to 0^{+}$ or $x \to 1$.

[1] Pre-calibrated CRF of a Cannon G5 camera in standard mode is used.

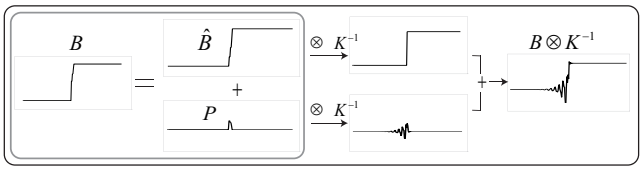

Fig. 5. Given an invertible filter, the ringing artifacts of a step edge is caused by the deconvolution of blur inconsistency P introduced by nonlinear CRF in Equation (18).

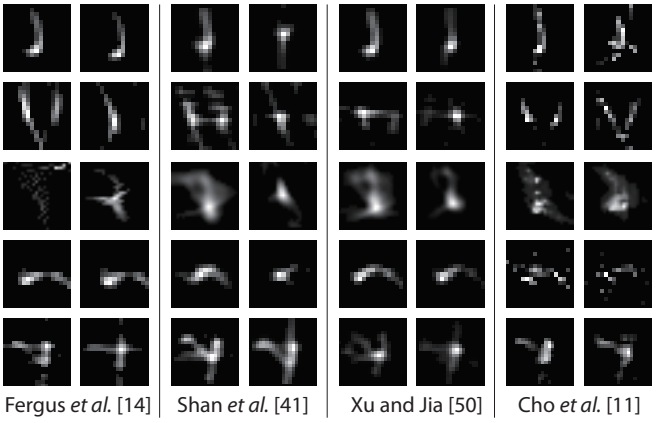

Fig. 6. This figure shows examples of PSF kernels from several images with linear CRF (left columns) or nonlinear CRF (right columns). PSF kernels in the same row are from the same image with different estimated methods: Fergus *et al.* [14]; Shan *et al.* [41]; Xu and Jia [50]; Cho *et al.* [11].

Therefore, P only has non-zero values in the blurred edge regions. Assuming an invertible filter K which has non-zero entries in frequency domain, we can represent the deconvolution of B with K by $B \otimes K^{-1}$, and thus

$$B \otimes K^{-1} = \widehat{B} \otimes K^{-1} + P \otimes K^{-1}, \tag{18}$$

where $\widehat{B} \otimes K^{-1} = I$ (Equation (4)). Thus, $P \otimes K^{-1}$ is the deconvolution artifacts introduced by the Blur Inconsistency Γ. Notice that even the blur inconsistency appears only within the edge areas, the deconvolution process can propagate the blur inconsistency errors from edge regions to smooth regions. Figure 5 illustrates the effects of decomposition in Equation (18). Again, the CRF plays a significant role in quality of the image deblurring.

B. Effects on PSF estimation

We also analyze the effects of a CRF on the PSF estimation by comparing the estimated PSF between a linear and nonlinear CRF. We show the estimated PSFs from Fergus *et al.* [14], Shan *et al.* [41], Xu and Jia [50] and Cho *et al.* [11] in Figure 6. The raw images from [11] were used for our testing purpose.

Ideally, the CRF should only affect the relative intensity of a PSF, but the shape of a PSF should remain the same since the shape of the PSF describes the trajectory of motion causing the motion blur, and the intensity of the PSF describes the relative speed of the motion. However, as we can observe in Figure 6, the estimated PSFs are noticeably different, especially for the results from [14] and [41]. This is because both [14] and [41] use alternating optimization for their non-blind deconvolution. As previously discussed, the nonlinear CRF causes errors during the deconvolution process which in turn propagates the errors

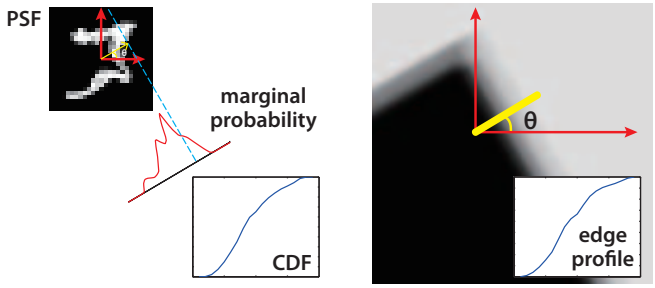

Fig. 7. This figure shows how the edge profile of a step edge in a motion blurred image is equal to the cumulative distribution function of the marginal probability of the motion blur kernel along the direction perpendicular to the edge.

to the estimated PSF in an alternating optimization framework. The results from [50] and [11] contains less errors because they separate the process of PSF estimation and image deconvolution. However, the shape of the estimated PSF are still different. The method in [50] requires edge selection and sharpening, and the method in [11] requires edge profiles to be aligned. Since the nonlinear CRF alters the edge profiles in the blurred image, their estimated PSF also contains errors inherent from non-uniform edge profiles. Note that small errors in the PSF estimation can causes significant artifacts in subsequent deconvolution.

V. CRF Estimation from a Blurred Image

In this section, we describe a method to estimate the CRF from one or more blurred images. To begin, we examine the relationship between the PSF and edge profiles in a blurred image under a linear CRF assumption. We then describe a method to estimate the CRF based on this relationship using least-squares fitting assuming a known PSF. This method is then converted to a robust estimation of an unknown PSF and a CRF using rank minimization.

A. PSF and edge profiles

We begin with the observation that the shape of a blur profile with the linear CRF resembles the shape of the cumulative distribution of the 1D PSF as shown in Figure 3 (a)(c). Our analysis is similar in fashion to that in [18] which used alpha mattes of blurred object to estimate the PSF. Our approach, however, works directly from the image intensities and requires no matting or object extraction. Instead, we only need to identify the step edges with homogeneous areas on both sides. For such edges, the shape of the blur profile is equal to the shape of the cumulative distribution of the 1D PSF.

Theorem 2. *Under a 1D motion blur, if the CRF is linear and the original edge in clear image is a step edge with uniform intensity on both sides, the shape of the blur profile is equal to the shape of the cumulative distribution of the 1D PSF.*

Proof: Consider a simple case where the original step edge has values $[0, \ldots, 0, 1, \ldots, 1]$ and the values of the PSF is $[\alpha_1, \alpha_2, \ldots, \alpha_M]$. If the number of 0's and 1's are both larger than M, the blur profile after the motion blur is equal to $[\alpha_1, \alpha_1 + \alpha_2, \ldots, \sum_{i=1}^{M} \alpha_i]$, which is the cumulative distribution of the 1D PSF.

For any edges with intensities $[I_1, I_2]$, the value of the blur profile at $m \in [1, \ldots, M]$ after the blur is equal to $I_1 + \sum_{i=1}^{m} \alpha_i (I_2 - I_1)$. ■

Theorem 2 is valid under the assumptions that the motion blurred image does not contain any noise or quantization error.

In the case of a 2D PSF, Theorem 2 still holds when the edge is a straight line. In this case, the 1D PSF becomes the marginal probability of the 2D PSF projected onto the line perpendicular to the edge direction as illustrated in Figure 7.

B. CRF approximation with a known PSF

Considering that the shape of blurred edge profiles are equal to the shape of the cumulative distribution of the PSF[2] if the CRF is linear. Given that we know the PSF, we can compute the CRF as follows:

$$\begin{aligned}\arg\min_{g(\cdot)} \quad & \sum_{j=1}^{E_1}\sum_{m=1}^{M} w_j \left(\frac{g(I_j(m)) - l_j}{w_j} - \sum_{i=1}^{m} \alpha_i \right)^2 \\ + \quad & \sum_{j=1}^{E_2}\sum_{m=1}^{M} w_j \left(\frac{g(I_j(m)) - l_j}{w_j} - \sum_{i=m}^{M} \alpha_i \right)^2, \end{aligned} \quad (19)$$

where $g(\cdot) = f^{-1}(\cdot)$ is the inverse CRF function, E_1 and E_2 are the numbers of selected blurred edge profiles from dark to bright regions and from bright region to dark regions, respectively.

The variables l_j and w_j are the minimum intensity value and the intensity range (intensity difference between the maximum and the minimum intensity values) of the blurred edge profiles after applying the inverse CRF. Blur profiles that span a wider intensity range are weighted more because their wider dynamic range covers a larger portion of $g(\cdot)$, and therefore provide more information about the shape of $g(\cdot)$. We filtered out the edges with $w_j < 0.1$ since according to our blur inconsistency analysis in Section III, these low contrast edges does not provide much information for PSF estimation.

We follow the method in [49] and model the inverse CRF $g(\cdot)$ using a polynomial of degree $d = 5$ with coefficients a_p, *i.e.*, $g(I) = \sum_{p=0}^{d} a_p I^p$. The optimization is subject to boundary constraints $g(0) = 0$ and $g(1) = 1$, and a monotonicity constraint that enforces the first derivative of $g(\cdot)$ to be non-negative. Our goal is to find the coefficients a_p such that the following objective function is minimized:

$$\begin{aligned}\arg\min_{a_p} & \sum_{j=1}^{E_1}\sum_{m=1}^{M} w_j \left(\frac{\sum_{p=0}^{d} a_p I_j(m)^p - l_j}{w_j} - \sum_{i=1}^{m} \alpha_i \right)^2 \\ & + \sum_{j=1}^{E_2}\sum_{m=1}^{M} w_j \left(\frac{\sum_{p=0}^{d} a_p I_j(m)^p - l_j}{w_j} - \sum_{i=m}^{M} \alpha_i \right)^2 \\ & + \lambda_1 \left(a_0^2 + \left(\sum_{p=0}^{d} a_p - 1 \right)^2 \right) \\ & + \lambda_2 \sum_{r=1}^{L} H\left(\sum_{p=0}^{d} a_p \left(\left(\frac{r-1}{L} \right)^p - \left(\frac{r}{L} \right)^p \right) \right), \end{aligned} \quad (20)$$

where H is the Heviside step function for enforcing the monotonicity constraint, *i.e.*, $H = 1$ if $g(r) < g(r-1)$, or $H = 0$ otherwise and L is the maximum intensity level, *e.g.*255 for 8-bit color depth. The weights are fixed to $\lambda_1 = 100$ and $\lambda_2 = 10$, which control the boundary constraint and the monotonic constraint, respectively. The solution of Equation (20) can be obtained by a simplex search method of Lagarias *et al.* [27][3].

C. CRF estimation with unknown PSF

Using the cumulative distribution of the PSF can reliably estimate the CRF under ideal conditions. However, the PSF is usually unknown in practice. As we have studied in Section IV-B, nonlinear CRF affects the accuracy of the PSF estimation, which in turn will affect our CRF estimation described in Section V-B. In this section, we introduce a CRF estimation method without explicitly computing the PSF.

As previously discussed, we want to find an inverse response function $g(\cdot)$ that makes the blurred edge profiles have the same shape after applying the inverse CRF. This can be achieved by minimizing the distance between each blur profile to the average blur profile:

$$\begin{aligned}\arg\min_{g(\cdot)} \quad & \sum_{j=1}^{E_1}\sum_{m=1}^{M} w_j \left(\frac{g(I_j(m)) - l_j}{w_j} - A_1(m) \right)^2 \\ + \quad & \sum_{j=1}^{E_2}\sum_{m=1}^{M} w_j \left(\frac{g(I_j(m)) - l_j}{w_j} - A_2(m) \right)^2, \end{aligned} \quad (21)$$

where $A_1(m) = \sum_{k=1}^{E_1} \frac{w_k}{W} g(I_k(m))$ is the weighted average blur profile, and $W = \sum_{l=1}^{E_1} w_l$ is a normalization factor.

Using the constraint in Equation (21), we can compute the CRF, however, this approach is unreliable not only because the constraint in Equation (21) is weaker than the constraint in Equation (19), but the nature of least-squares fitting is sensitive to outliers. To avoid these problems, we generalize our method to robust estimation via rank minimization.

Recall that the edge profiles should have the same shape after applying the inverse CRF. This means that if the CRF is linear, the edge profiles are linearly dependent with each other, and hence the observation matrix of edge profiles form a rank-1 matrix for *each* group of edge profiles:

$$g(\mathcal{M}) = \begin{pmatrix} g(I_1(1)) - l_1 & \cdots & g(I_1(M)) - l_1 \\ \vdots & \ddots & \vdots \\ g(I_{E_1}(1)) - l_{E_1} & \cdots & g(I_{E_1}(M)) - l_{E_1} \end{pmatrix}, \quad (22)$$

where M is length of edge profiles, and E_1 is the number of observed edge profiles grouped according to the orientation of edges. Now, we transform the problem into a rank minimization problem which finds a function $g(\cdot)$ that minimizes the rank of the observation matrix $\mathcal{M}$ of edge profiles. Since the CRF is the same for the whole image, we define our objective function for rank minimization as follow:

$$\arg\min_{g(\cdot)} \sum_{k=1}^{K} w_k \text{rank}(g(\mathcal{M}_k)), \quad (23)$$

where K is total number of observation matrix (total number of group of edge profiles), w_k is a weight given to each observation matrix. We assign larger weight to the observation matrix that contains more edge profiles. Note that Equation (23) is also applicable to multiple images since the observation matrix is built individually for each edge orientation and for each input image.

[2]For simplicity, we assume that the PSF is 1D, and it is well aligned with the edge orientation. If the PSF is 2D, we can compute the marginal probability of the PSF.

[3]`fminsearch` function in Matlab.

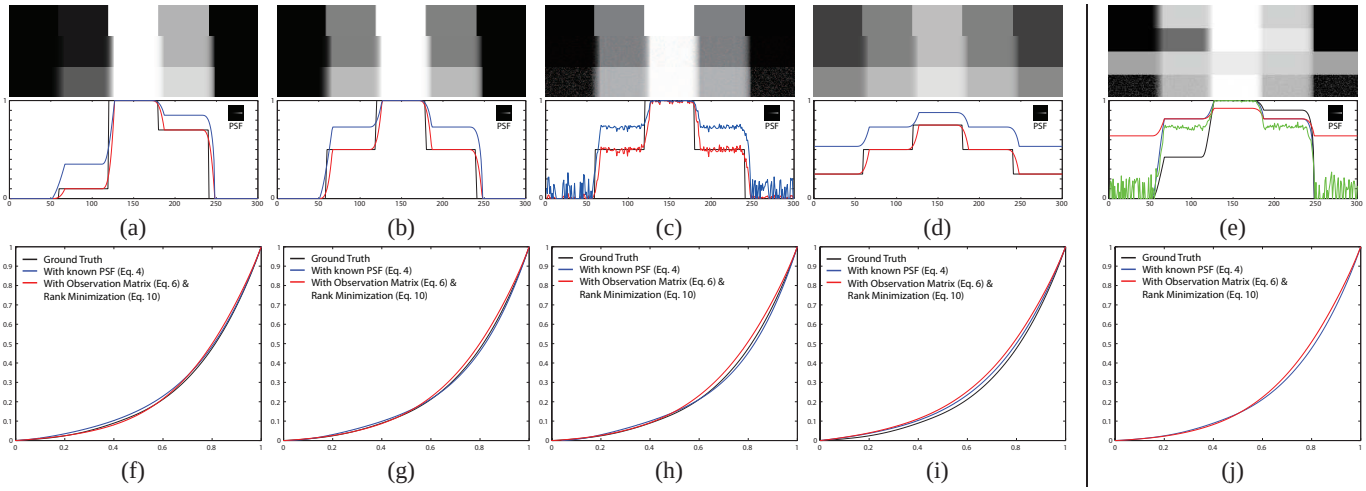

Fig. 8. We test the robustness of our CRF estimation method under different configurations. (a) Blur profiles with different intensity ranges, (b) edges in the original image contains mixed intensities (edge width is equal to 3 pixels), (c) Gaussian noise ($\sigma = 0.02$) is added according to Equation (2), (d) the union of intensity range of all blur profiles does not cover the whole CRF curve. (e) Blur profiles of (a), (b), (c), (d). The original image (black lines), the blurred image with linear CRF (red lines), and the blurred image with nonlinear CRF (blue lines) are shown on top of each figure in (a)-(d). (f)-(i) the corresponding estimated inverse CRF using our methods with (a)-(d). (j) the corresponding estimated inverse CRF with multiple images in (e).

We evaluate the rank of matrix $\mathcal{M}$ by measuring the ratio of its singular values:

$$\arg\min_{g(\cdot)} \sum_{k=1}^{K} w_k \sum_{j=2}^{E_k} \frac{\sigma_{kj}}{\sigma_{k1}}, \tag{24}$$

where σ_{kj} are the singular values of $g(\mathcal{M})_k$. If the observation matrix is rank-1, only the first singular values is nonzero and hence minimizes Equation (24). In our experiments, we found that Equation (24) can be simplified to just measuring the ratio of the first two singular values:

$$\arg\min_{g(\cdot)} \sum_{k=1}^{K} w_k \frac{\sigma_{k2}}{\sigma_{k1}}. \tag{25}$$

Combining the monotonic constraint, the boundary constraint and the polynomial function constraint from Equation (20), we obtain our final objective function:

$$\begin{aligned} \arg\min_{a_p} \sum_{k=1}^{K} w_k \frac{\sigma_{k2}}{\sigma_{k1}} + \lambda_1 \left(a_0^2 + \left(\sum_{p=0}^{d} a_p - 1 \right)^2 \right) \\ + \lambda_2 \sum_{r=1}^{L} H \left(\sum_{p=0}^{d} a_p \left(\left(\frac{r-1}{L} \right)^p - \left(\frac{r}{L} \right)^p \right) \right). \end{aligned} \tag{26}$$

Equation (26) can be solved effectively using nonlinear least-squares fitting[4].

D. Implementation issues for 2D PSF

Our two proposed methods for CRF estimation are based on the 1D blur profile analysis. Since, in practice, PSFs are 2D in nature, we need to group image edges with similar orientation and select valid edge samples for building the observation matrix. We use the method in [11] to select the blurred edges. The work in [11] filtered edge candidates by keeping only high contrast straight-line edges. A user parameter controls the minimum length of straight-line edges which depends on the size of the PSF. We refer to [11] for details of selecting high contrast straight-line edges in blurry images.

[4] `lsqnonlin` function in Matlab.

Fig. 9. Our selected edges for CRF estimation. Edges are grouped according to the edge orientation (color coded). The estimated CRF and the deblurred images are shown in Figure 12.

After selecting valid edge profiles, they are grouped according to edge orientations. Figure 9 shows examples of the selected edges and the grouping results. The selected edges were grouped by selecting partitioning thresholds such that the orientation variation within each group is less than 2 degree. To increase the number of candidate edges within each group, edges in opposite direction were grouped together. When building the observation matrix in Equation (22), we reverse the CDF of the opposite edges by computing $\{1 - [g(I_j(1)) - l_j] \cdots 1 - [g(I_j(M)) - l_j]\}$. To make the selected edge profiles more robust against noise and outliers, we apply a 1D directional filter in a direction orthogonal to the edge orientation to get the local average of edge profiles. We found that this directional filtering improved the robustness of our edge selection algorithm even when the candidate edges were slightly curved.

After edge selection and grouping, edge profiles are aligned to build the observation matrix. In [11], edge profiles were aligned according to the center of mass. In our case, however, due to the nonlinear CRF effects, alignment based on the center of mass is not reliable. We instead align the two end points of the edges. In cases where the projected 1D PSF contains discontinuities, the starting and end points of the discontinuities are also considered in the alignment. Since the amount of blur in different directions

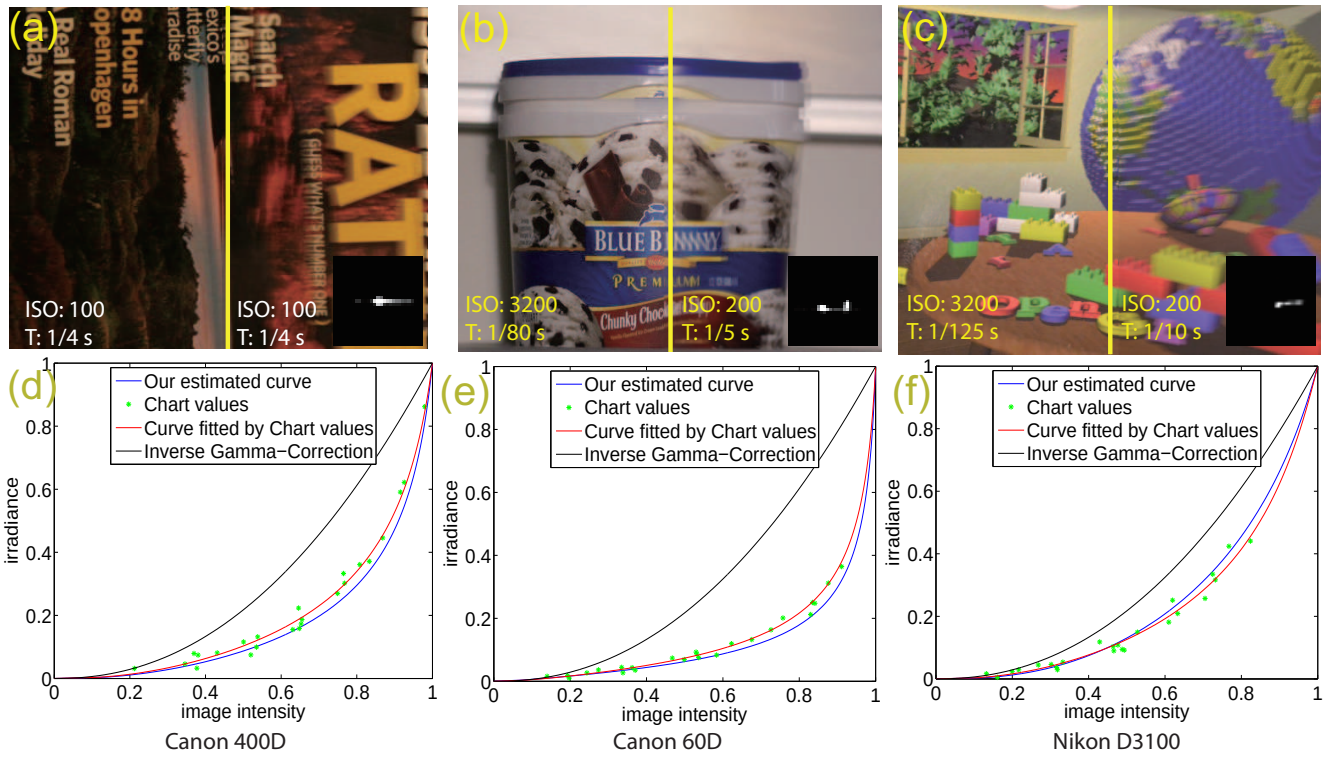

Fig. 10. CRF estimation on real images. The top row shows the sharp/blurred pairs. The bottom row shows our recovered the CRF (in blue) and the ground truth CRF (in red) obtained by acquiring the MacBeth's chart (in green).

varies according to the shape of the PSF, we give a larger weight to the directions with longer edge profiles as they provide more information about the CRF than sharp edges. When dealing with multiple images, the same weighting scheme applies where a larger weight is given to a more blurry edge profile.

Our rank minimization using nonlinear least-squares fitting is sensitive to the initial estimation of the CRF. In our implementation, we use the average CRF profile from the database of response functions (DoRF) created by Grossberg and Nayar [16] as our initial guess. The DoRF database contains 201 measured functions which allows us to obtain a good local minima in practice.

VI. Experimental results

In this section, we evaluate the performance of our CRF estimation method using both synthetic and real examples. In the synthetic examples, we test our algorithm under different conditions in order to better understand the behaviors and the limitations of our method. In the real examples, we evaluate our method by comparing the amount of ringing artifacts with and without CRF intensity correction to demonstrate the effectiveness of our algorithm and the importance of CRF in the context of image deblurring.

A. Synthetic examples

Figure 8 shows the performance of our CRF estimation under different conditions. We first test the effects of the intensity range of the blur profiles in Figure 8 (a). In a real application, it is uncommon that all edges will have a similar intensity range. These intensity range variations can potentially affect the estimated CRF as low dynamic range edges usually contain larger quantization errors. As shown in Figure 8 (f), our method is reasonably robust to these intensity range variations.

Our method assumes that the original edges are step edges. In practice, there may be color mixing effect even for an edge that is considered as a sharp edge. In our experiments, we find that the performance of our approach degrades quickly if the step edge assumption is violated. However, as shown in Figure 8 (g), our approach is still effective if the color mixing effects is less than 3 pixel wide given a PSF with size 15. The robustness of our method when edge color mixing is present depends on the size of the PSF with our approach being more effective for larger PSFs.

Noise is inevitable even when the ISO of a camera is high. We test the robustness of our method against image noise in Figure 8 (c). We add Gaussian noise to Equation (2) where the noise is added after the convolution process but before the CRF mapping. As can be observed in Figure 8 (h), the noise affects the accuracy of our method. In fact, using the model in Equation (2), we can observe that the noise has also captured some characteristics of the CRF. The magnitude of noise in the darker region is larger than the magnitude of noise in the brighter region. Such information may even be useful and combined into our framework to improve the performance of our algorithm as discussed in [36].

We test the sensitivity of our algorithm when the union of blur profiles does not cover the whole range of CRF. As can be seen in Figure 8 (i), our method still gives reasonable estimations. This is because the polynomial and monotonicity constraint assist in

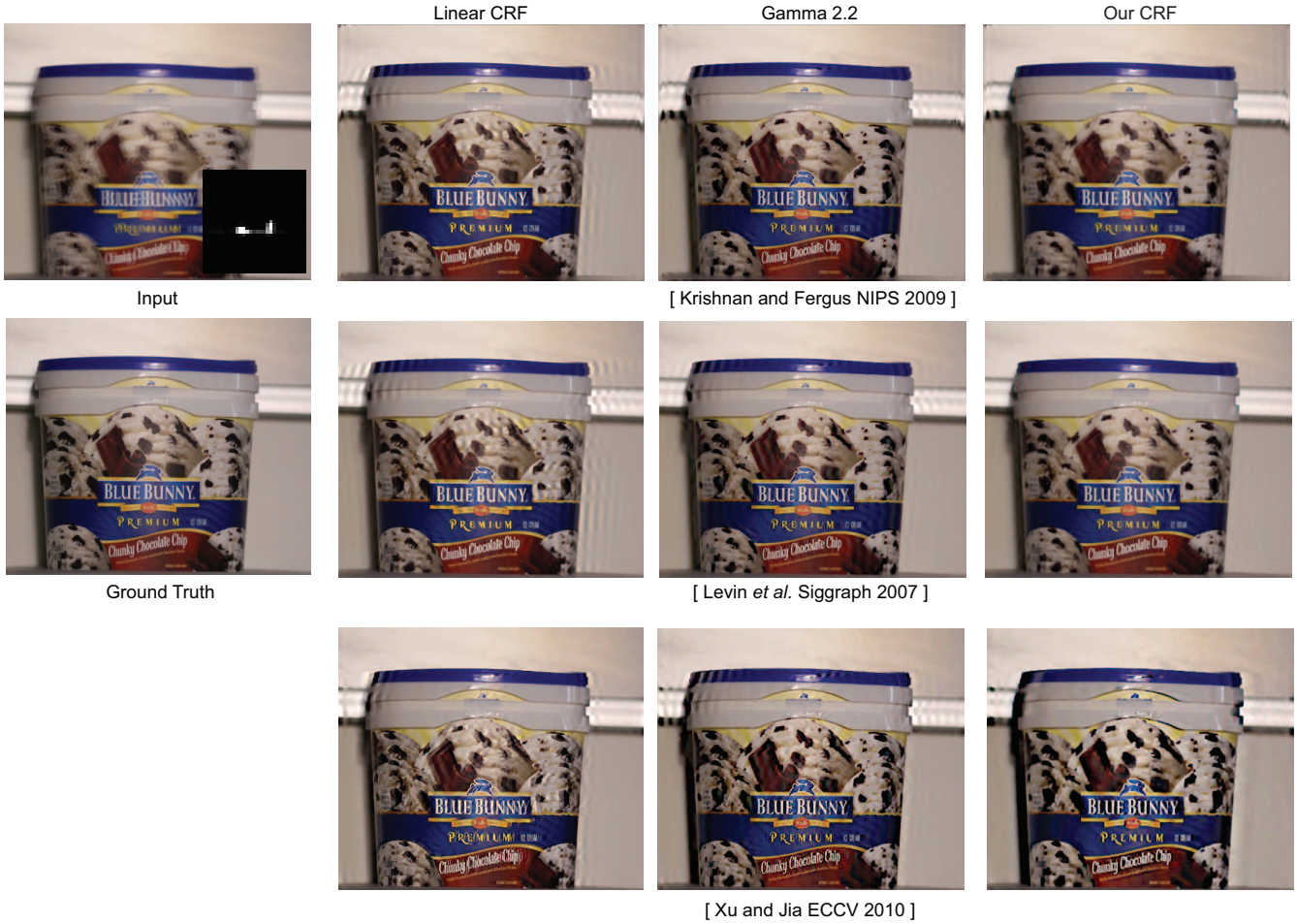

Fig. 11. Qualitative comparison on non-blind deconvolution results with linear CRF, gamma curve, and our estimated CRF correction. We show the results for three different state-of-the-art regularization based deconvolution method: Krishnan and Fergus [25], Levin *et al.* [30], and Xu and Jia [50]. The estimated CRF is shown in Figure 10. Among all of the compared results, our estimated CRF correction consistently performs better than gamma curve correction.

maintaining the shape of CRF. Note that having limited range of intensities will degrade the performance of all radiometric calibration methods.

Finally, we show a result where we use all input images to estimate the CRF. As expected, more input images give a more accurate CRF estimation.

The synthetic experiments show that the performance of our method depends on not only the quantity of the observed blur profiles but also the quality of the profiles. For instance, a blur profile with a large motion covering a wide intensity range is better than the combination of blur profiles that cover only a portion of intensity range. When combining the observations from multiple images, our estimated CRF is more accurate as the mutual information from different images increases the robustness of our algorithm. The rank minimization also makes our algorithm less sensitive to outliers.

B. Real examples

1) With Known PSF: To test our algorithm with a known PSF in real world examples, we implemented the method from [51] which uses a pair of blurry/sharp image to estimate a reliable motion PSF. Although we can use previous single image methods, *e.g.* [14], [41], [50], [11], to get the PSF, we found that the PSF from [51] is more reliable especially when the CRF is nonlinear (Section IV-B). We validated our approach on three different camera models: Canon 60D, 400D, and Nikon D3100.

Figure 10(a),(b) and (c) show the captured sharp/blurry image pairs. The ISO value and the relative exposure setting for each captured image pair were also shown. The sharp images were captured with a tripod whereas the blurry images were captured by holding the camera by hands with long exposure period. To obtain the ground truth CRF for comparisons, we used the Macbeth color checkerboard and applied the PCA-based method [15] to estimate f^{-1} via curve fitting [38]. Figure 10 (d),(e) and(f) plot our estimated CRFs against the ground truth CRFs. The green dots are the sampled chart values from the Macbeth color checkerboard.

Finally, we tested the effectiveness of different regularization-based deconvolution algorithms in Figure 11. In particular, we compare the method from Krishnan and Fergus [25], Levin *et al.* [30], and Xu and Jia [50]. The work from Krishnan and Fergus uses hyper-laplacian prior to regularize the deconvolved image, Levin *et al.*use the sparsity regularization while Xu and Jia use the L1-norm regularization. Among all the deconvolution results, the gamma correction consistently shows better results than the results using linear CRF correction. However, with our estimated CRF correction, the deconvolution results for all three methods

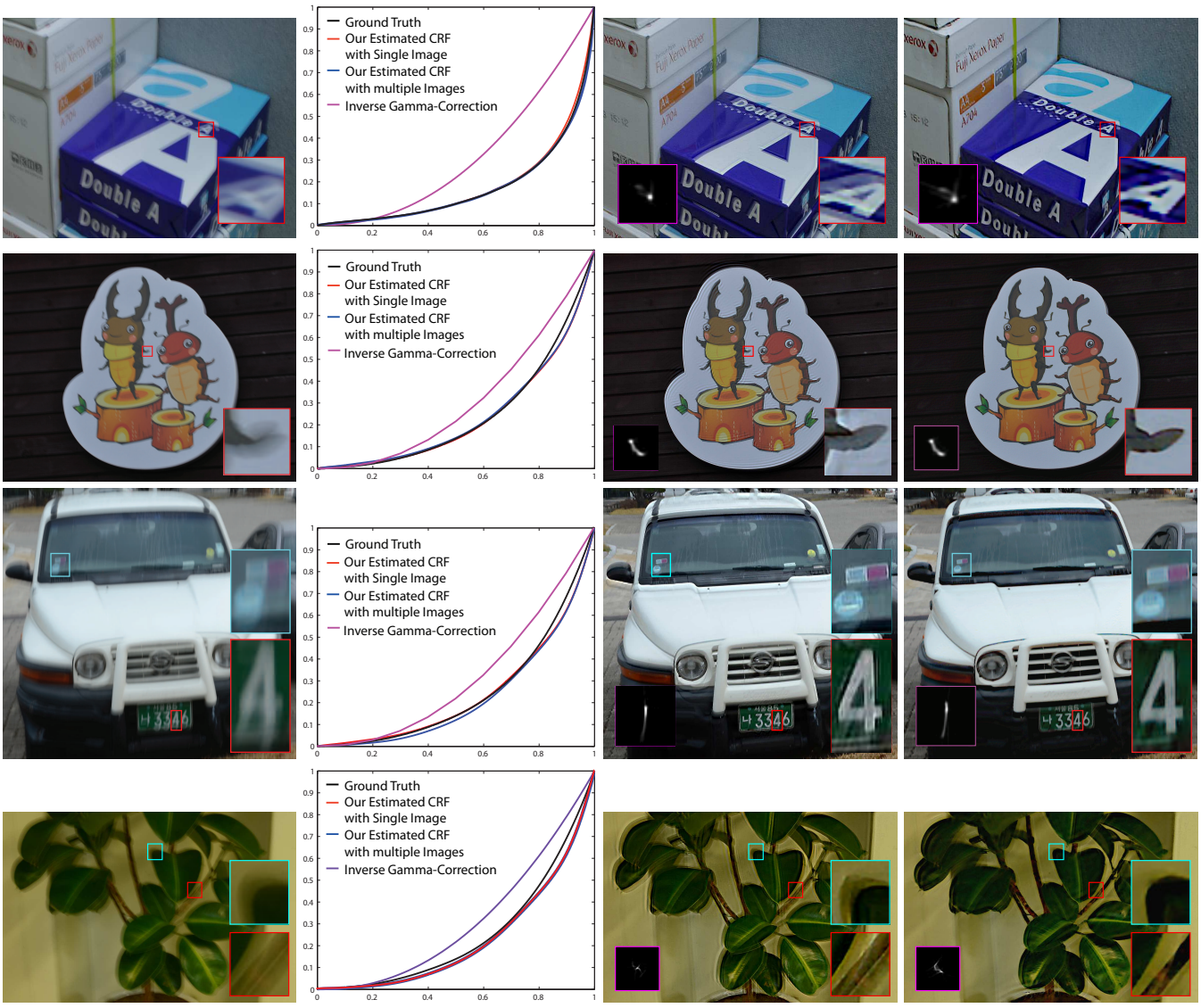

Fig. 12. Our result with real examples: (a) input images; (b) estimated CRFs; (c) deblurred images with gamma correction; (d) deblurred images with CRF correction.

can be further improved.

2) With Unknown PSF: When the PSF is not available, we estimate the inverse CRF using the method in Section V-C. Note that since the CRF estimation step is separated from the PSF estimation step, the accuracy of our estimated CRF for the real examples does not depend on the PSF estimation algorithm. In our implementation, we choose the method in [50] to estimate the PSF from a single image and the method in [30] with the sparsity regularization for deconvolution.

Figure 12 shows the results from the input image in (a) that is captured by a Canon EOS 400D (first row) and a Nikon D90 DSLR (second and third rows) camera with a nonlinear CRF. The results in (b) are the estimated CRF using single and multiple images. The ground truth CRFs were computed by using method in [28] with a calibration pattern. For the reference, we have also show the inverse gamma-correction curve with γ equal to 2.2. This is a common method suggested by the previous deblurring algorithm [14] when the CRF is unknown. Note the shape of the inverse gamma-correction curve is very different from the shape of ground truth and our estimated CRF. We compare the results with gamma correction ($\gamma = 2.2$) and with our estimated CRF corrections in (c) and (d) respectively. As expected, our results with CRF corrections are better – not only do the deblurring results contain less artifacts, but the estimated PSFs are also more accurate after the CRF correction.

VII. Discussion

A. Effectiveness of Gamma Correction

When the ground truth CRF is unknown, a common method in previous deblurring algorithms [14], [50] is to use gamma curve correction with $\gamma = 2.2$. In this section, we provide additional analysis to the effectiveness of this approach. Let the blurred irradiance be $\tilde{B} = \tilde{I} \otimes K$, and the observed intensity be $B = f(\tilde{B})$. When gamma curve is used, we have:

$$f_g{}^{-1}(f(\tilde{B})) = f(\tilde{B})^{2.2}, \tag{27}$$

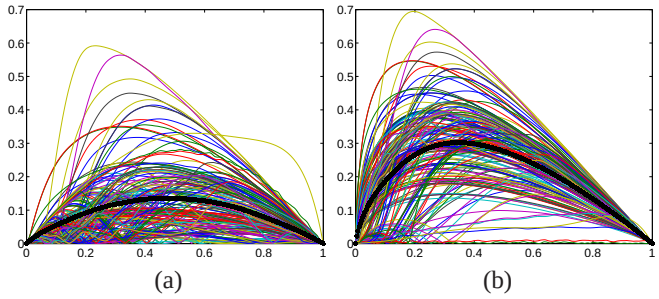

Fig. 13. The error curves of DoRF CRFs when (a) gamma curve ($\gamma = 2.2$) and (b) linear CRF are used to approximate the ground truth CRFs. The horizontal axis denotes the $\tilde{B}$ values, and the vertical axis denotes the error $\tau(\tilde{B})$. The colors of these curves represent different underlying CRFs. The central dark curve shows the mean τ for all the 188 real CRFs.

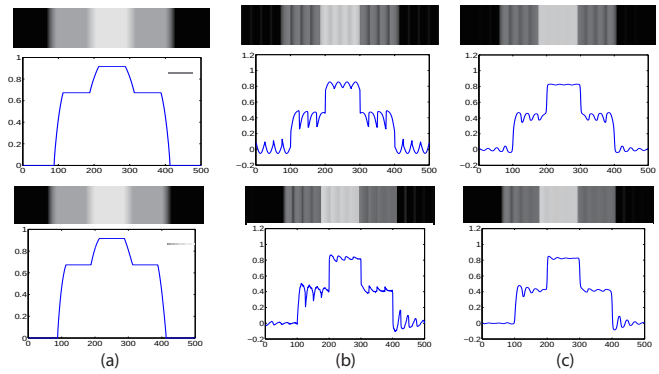

Fig. 14. We tested the effectiveness of gamma correction on synthetic example. (a) Input synthetic signal. Deconvolution with gamma curve correction using (b) wiener filter, and (c) sparsity regularization [30]. As discussed in Section IV, the ringing artifacts are mainly caused by the blur inconsistency. The gamma curve correction cannot fully eliminate blur inconsistency especially for edges with high contrast.

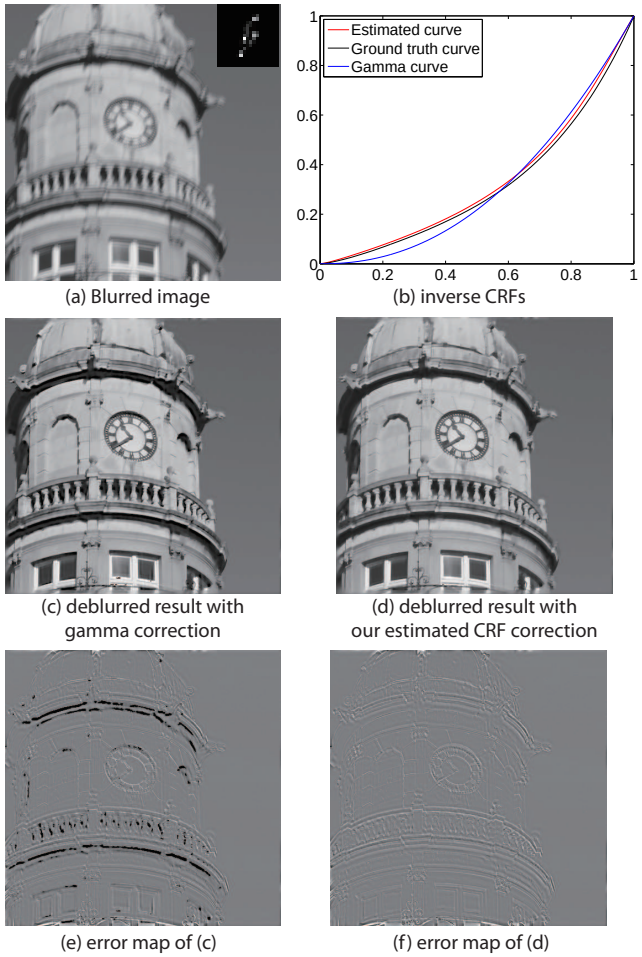

Fig. 15. (a) Input blurred Image. (b) The inverse CRFs. Note the gamma curve with $\gamma = 2.2$ is closed to the inverse of mean CRFs. (c) Deblurred image with gamma curve correction. (d) Deblurred image with our estimated inverse CRF correction. (e) Error maps using gamma correction. (f) Error maps using our estimated CRF correction.

where $f_g(x) = x^{1/2.2}$ denotes the gamma curve CRF. Thus, the absolute error introduced by the curve can be measured by:

$$\tau(\tilde{B}) = |f(\tilde{B})^{2.2} - \tilde{B}|. \tag{28}$$

As discussed previously in Section III and Section IV, errors in the CRF estimation will be directly transferred to the deblurred image leading to large ringing artifacts that cannot fully be suppressed by regularization.

In order to show the magnitude of the approximation errors, we measure the differences between the gamma curve and the 188 real CRF database [15] presented in Figure 2. Figure 13(a) shows the approximation errors of the gamma curve. The central dark curve shown in the figure represents the mean of the error $\tau(\tilde{B})$ for all the 188 real CRF curves. Note that most part of the error curves have errors larger than 0.1 which is 10% of intensity range. Some curves even have errors as large as 0.6. For the reference, we also show the approximation errors if a linear CRF is used in Figure 13(b). Although the gamma curve has smaller errors compared to the linear CRF, gamma curve is insufficient to represent the real-world CRFs as noted in previous work [15], [31], [23].

Next, we use the synthetic examples in Figure 3 to analyze the effectiveness of gamma curve correction in the non-blind deconvolution. Figure 14 shows the result. The gamma curve correction can reduce errors compared to the results using the linear correction, and the ringing artifacts are further reduced when a regularization-based deconvolution is used. Yet, as illustrated in Figure 14, it cannot completely remove the ringing artifacts caused by the blur inconsistency from nonlinear CRF.

Finally, we show an example in Figure 15, where the gamma curve correction is "successful". We use the mean CRF of the 188 real CRF database [15] as the ground truth CRF. As illustrated in Figure 15(b), the gamma curve with $\gamma = 2.2$ is closed to the inverse of mean CRFs. We use the method in Section V-B to estimate the CRF with known PSF. This example is considered as successful in deblurring since the deconvolution artifacts are small and unnoticeable after a regularization is used. However, if we compare the error maps between the gamma curve correction and our estimated CRF correction, our approach can further reduce errors with the same deconvolution algorithm [25].

B. Assumptions and Limitations

Our proposed algorithms algorithms work under several assumptions. In the following, we analyze each of the assumptions and discuss the limitations of our approach in practise.

1) Robustness against image noise: Theorem 2 for our CRF estimation algorithms assumes noise-free conditions. To analyze

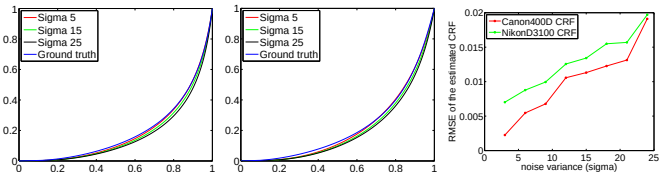

Fig. 16. The estimated CRF under different noise level. (a) Canon400D. (b) Nikon D3100. (c) Plot of RMSE of the estimated CRF against different amount of noise.

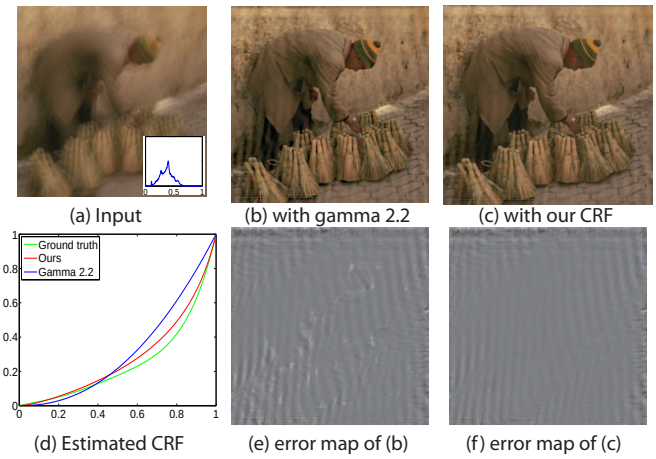

Fig. 17. Failure case. Our algorithm fails to estimate accurate CRF when the intensity range of input image is narrow. Yet, the deblurred result is still better than the gamma curve with less ringing artifacts.

the robustness of our algorithms against image noise, we generate a set of synthetic blurry and noisy images with different amount of Gaussian noise. The ground truth image in Figure 15 and the CRF curves of Canon400D and Nikon D3100 were used to produce the synthetic inputs. Figure 16 shows the plot of RMSE of the estimated CRF (with unknown PSF) against different amount of noise. Our CRF estimation algorithm is robust to image noise thanks to the usage of rank minimization optimization and the directional filtering in the edge selection step.

2) Spatially varying blur: Our CRF estimation algorithms assume spatially invariant motion blur. When facing spatially varying motion blur or defocus blur with different depth layers, the blind CRF estimation algorithm with unknown PSF will break down since the observation matrix is no longer a rank-1 matrix. In such scenario, only the CRF estimation algorithm with known PSF can be used providing that the local PSF can be obtained accurately. The blur inconsistency analysis, however, should still hold which claims that the irradiance of the blurry image should be linearized before deblurring in order to avoid ringing artifacts caused by non-linear CRF.

3) Failure Cases: We finally provide a failure case in Figure 17 where the CRF estimation fails due to the narrow intensity range of the input image. The estimated CRF deviates from the ground truth CRF especially for the area that is not covered by the intensity range of input image. However, when comparing deblurring results using a gamma curve, our result is still better with less ringing artifacts. As discussed earlier, the goal of this paper is to provide a method to handle nonlinear CRF in deblurring problem when the ground truth CRF is not accessible. In some cases, even an incorrectly estimated CRF may produce better deblurring results than not performing linearization at all.

The blur inconsistency analysis in Section III assumes a convex CRF. In practice, there are camera models where the CRF is non-convex in shape especially for the blue channel. We tested our algorithms for non-convex CRF using synthetic examples. However, we found that our estimated CRFs for unknown PSF are not as accurate as the convex cases. One possible explanation is that the non-convex CRFs deviate enough from the mean CRF to cause the nonlinear least-squares fitting in the rank minimization to converge to an incorrect local minima.

We have also tested our algorithms for highly textured images where straight-line edges are very limited. Both algorithms failed since the edge detection algorithm fail to detect straight-line edges. We consider this is a fundamental limitation to our algorithms.

VIII. Conclusion

This paper offers two contributions targeting image deblurring in the face of nonlinear CRFs. First, we have presented an analysis on the role that nonlinear CRFs play in image deblurring. We prove that the blur inconsistency introduced by nonlinear CRF can caused notable ringing artifacts in the deconvolution process which cannot be completely ameliorated by image regularization. Such blur inconsistency is spatially varying and it depends on edge sharpness, edge intensity range, and image brightness. We have also demonstrated how the nonlinear CRF adversely affects PSF estimation for several state-of-the-art techniques.

In Section V, we prove how the shape of edge projections resemble the cumulative distribution function of 1D PSFs for linear CRFs. This theorem was used to formulate two CRF estimation strategies for when the motion blur PSF kernel is known or not known. In the latter case, we show how rank minimization can be used to provide a robust estimation. We do note that our approach is sensitive to the quality of the selected blur profiles. The requirement of straight line sharp edges also places a limitation to our current solution. To this end, we have also provided a multiple image solution in case a motion blurred image does not contains sufficient edge profiles for CRF estimation.

Experimental results in real examples demonstrated the importance of intensity linearization in the context of image deblurring. In addition, we have analyzed the effectiveness of gamma curve correction which is commonly used in previous deblurring algorithms [14], [50]. The shape of gamma curve with $\gamma = 2.2$ is close to the inverse of mean CRFs. Therefore, in most cases, gamma curve correction is more effective than linear CRFs. However, when compared to the results with our estimated CRF corrections, gamma curve correction is still insufficient especially when the CRF is largely deviate from the mean CRFs.

IX. Acknowledgement

This work was funded in part by the National Research Foundation (NRF) of Korea (2012-0003359), Microsoft Research Asia under the KAIST-Microsoft Research Collaboration Center (KMCC), Natural Science Foundation (China) (Nos:61273258, 61105001), the Committee of Science and Technology, Shanghai (No. 11530700200), National Science Foundation (US) under grants IIS-CAREER-0845268 and IIS-RI-1016395, the Air Force Office of Science Research under the YIP Award, and the Singapore A*STAR PSF grant (Proj No. 1121202020).

REFERENCES

[1] M. Ben-Ezra and S. Nayar. Motion-based Motion Deblurring. *IEEE Trans. PAMI*, 26(6):689–698, Jun 2004.
[2] J. Cai, H. Ji, C. Liu, and Z. Shen. Blind motion deblurring from a single image using sparse approximation. In *CVPR*, 2009.
[3] A. Chakrabarti, D. Scharstein, and T. Zickler. "an empirical camera model for internet color vision". In *BMCV*, 2009.
[4] Y. Chang and J. Reid. Rgb calibration for color image-analysis in machine vision. *IEEE Trans. Image Processing*, 5(10):14141422, 1996.
[5] J. Chen and C. K. Tang. Robust dual motion deblurring. In *CVPR*, 2008.
[6] X. Chen, X. He, J. Yang, and Q. Wu. An effective document image deblurring algorithm. In *CVPR*, 2011.
[7] X. Chen, F. Li, J. Yang, and J. Yu. A theoretical analysis of camera response functions in image deblurring. In *ECCV*, 2012.
[8] S. Cho and S. Lee. Fast motion deblurring. In *ACM SIGGRAPH ASIA*, 2009.
[9] S. Cho, Y. Matsushita, and S. Lee. Removing non-uniform motion blur from images. In *ICCV*, 2007.
[10] S. Cho, J. Wang, and S. Lee. Handling Outliers in Non-blind Image Deconvolution. In *ICCV*, 2011.
[11] T.-S. Cho, S. Paris, B. Freeman, and B. Horn. Blur kernel estimation using the radon transform. In *CVPR*, 2011.
[12] P. Debevec and J. Malik. Recovering high dynamic range radiance maps from photographs. In *ACM SIGGRAPH*, 1997.
[13] H. Farid. Blind inverse gamma correction. *IEEE Trans. Image Processing*, 10(10):14281433, 2001.
[14] R. Fergus, B. Singh, A. Hertzmann, S. T. Roweis, and W. T. Freeman. Removing camera shake from a single photograph. *ACM Trans. Graph.*, 25(3), 2006.
[15] M. Grossberg and S. Nayar. Modeling the space of camera response functions. *IEEE Trans. PAMI*, 26(10), 2004.
[16] M. D. Grossberg and S. K. Nayar. What is the space of camera response functions? In *CVPR*, 2003.
[17] M. Hirsch, C. Schuler, S. Harmeling, and B. Schölkopf. Fast removal of non-uniform camera shake. In *ICCV*, 2011.
[18] J. Jia. Single image motion deblurring using transparency. In *CVPR*, 2007.
[19] N. Joshi, S. Kang, L. Zitnick, and R. Szeliski. Image deblurring with inertial measurement sensors. *ACM Trans. Graph.*, 29(3), 2010.
[20] N. Joshi, R. Szeliski, and D. Kriegman. Psf estimation using sharp edge prediction. In *CVPR*, 2008.
[21] S. Kim, J. Frahm, and M. Pollefeys. Radiometric calibration with illumination change for outdoor scene analysis. In *CVPR*, 2008.
[22] S. Kim, Y.-W. Tai, S. Kim, M. S. Brown, and Y. Matsushita. Nonlinear camera response functions and image deblurring. In *CVPR*, 2012.
[23] S. J. Kim, H. T. Lin, Z. Lu, S. Susstrunk, S. Lin, and M. S. Brown. A new in-camera imaging model for color computer vision and its application. In *IEEE Trans. PAMI*, 2012.
[24] S. J. Kim and M. Pollefeys. Robust radiometric calibration and vignetting correction. *IEEE Trans. PAMI*, 30(4), 2008.
[25] D. Krishnan and R. Fergus. Fast image deconvolution using hyper-laplacian priors. In *NIPS*, 2009.
[26] D. Krishnan, T. Tay, and R. Fergus. Blind deconvolution using a normalized sparsity measure. In *CVPR*, 2011.
[27] J. Lagarias, J. Reeds, M. Wright, and P. Wright. Convergence properties of the nelder-mead simplex method in low dimensions. *SIAM Journal of Optimization*, 9(1):112–147, 1998.
[28] J.-Y. Lee, B. Shi, Y. Matsushita, I. Kweon, and K. Ikeuchi. Radiometric calibration by transform invariant low-rank structure. In *CVPR*, 2011.
[29] A. Levin. Blind motion deblurring using image statistics. In *NIPS*, 2006.
[30] A. Levin, R. Fergus, F. Durand, and W. T. Freeman. Image and depth from a conventional camera with a coded aperture. *ACM Trans. Graph.*, 26(3), 2007.
[31] H. Lin, S. J. Kim, S. Susstrunk, and M. S. Brown. Revisiting radiometric calibration for color computer vision. In *ICCV*, 2011.
[32] S. Lin, J. Gu, S. Yamazaki, and H.-Y. Shum. Radiometric calibration from a single image. In *CVPR*, 2004.
[33] S. Lin and L. Zhang. Determining the radiometric response function from a single grayscale image. In *CVPR*, 2005.
[34] P.-Y. Lu, T.-H. Huang, M.-S. Wu, Y.-T. Cheng, and Y.-Y. Chuang. High dynamic range image reconstruction from hand-held cameras. In *CVPR*, 2009.
[35] L. Lucy. An iterative technique for the rectification of observed distributions. *Astron. J.*, 79, 1974.
[36] Y. Matsushita and S. Lin. Radiometric calibration from noise distributions. In *CVPR*, 2007.
[37] T. Mitsunaga and S. Nayer. Radiometric self calibration. In *CVPR*, 1999.
[38] T.-T. Ng, S.-F. Chang, and M.-P. Tsui. Using geometry invariants for camera response function estimation. In *CVPR*, 2007.
[39] A. Rav-Acha and S. Peleg. Two motion blurred images are better than one. *PRL*, 26:311–317, 2005.
[40] W. Richardson. Bayesian-based iterative method of image restoration. *J. Opt. Soc. Am.*, 62(1), 1972.
[41] Q. Shan, J. Jia, and A. Agarwala. High-quality motion deblurring from a single image. *ACM Trans. Graph.*, 2008.
[42] Y.-W. Tai, H. Du, M. Brown, and S. Lin. Image/video deblurring using a hybrid camera. In *CVPR*, 2008.
[43] Y.-W. Tai, H. Du, M. S. Brown, and S. Lin. Correction of spatially varying image and video motion blur using a hybrid camera. *IEEE Trans. PAMI*, 32(6):1012–1028, 2010.
[44] Y.-W. Tai, N. Kong, S. Lin, and S. Shin. Coded exposure imaging for projective motion deblurring. In *CVPR*, 2010.
[45] Y.-W. Tai and S. Lin. Motion-aware noise filtering for deblurring of noisy and blurry images. In *CVPR*, 2012.
[46] Y.-W. Tai, P. Tan, and M. Brown. Richardson-lucy deblurring for scenes under projective motion path. *IEEE Trans. PAMI*, 33(8):1603–1618, 2011.
[47] O. Whyte, J. Sivic, A. Zisserman, and J. Ponce. Non-uniform deblurring for shaken images. In *CVPR*, 2010.
[48] N. Wiener. Extrapolation, interpolation, and smoothing of stationary time series. *New York: Wiley*, 1949.
[49] B. Wilburn, H. Xu, and Y. Matsushita. Radiometric calibration using temporal irradiance mixtures. In *CVPR*, 2008.
[50] L. Xu and J. Jia. Two-phase kernel estimation for robust motion deblurring. In *ECCV*, 2010.
[51] L. Yuan, J. Sun, L. Quan, and H. Shum. Image deblurring with blurred/noisy image pairs. *ACM Trans. Graph.*, 26(3), 2007.

Yu-Wing Tai received the BEng (first class honors) and MS degrees in compute science from the Hong Kong University of Science and Technology (HKUST) in 2003 and 2005 respectively, and the PhD degree from the National University of Singapore (NUS) in June 2009. He joined the Korea Advanced Institute of Science and Technology (KAIST) as an assistant professor in Fall 2009. He regularly serves on the program committees for the major Computer Vision conferences (ICCV, CVPR, and ECCV). His research interests include computer vision and image/video processing. He is a member of the IEEE.

Xiaogang Chen is currently a PhD student in the Institute of Image Processing and Pattern Recognition, Shanghai Jiao Tong University. His research interests include image and video processing, and computer vision. He is a student member of the IEEE.

Sunyeong Kim received the BS and MS degrees in Computer Science from Korea Advanced Institute of Science and Technology (KAIST) in 2010 and 2012 respectively. She is currently pursuing the PhD degree in KAIST. Her research interests include computer vision and image/video processing, especially in computational photography. She is a student member of the IEEE.

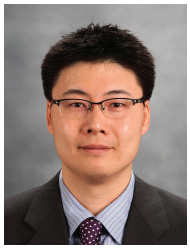

Seon Joo Kim received the BS and MS degrees from Yonsei University, Seoul, Korea, in 1997 and 2001. He received the PhD degree in computer science from the University of North Carolina at Chapel Hill in 2008. He is an assistant professor at the Department of Computer Science, Yonsei University since March 2013. His research interests include computer vision, computer graphics/computational photography, and HCI/visualization. He is a member of the IEEE.

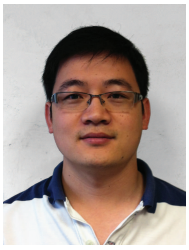

Feng Li received his BE from the Department of Electrical Engineering, Fuzhou University, in 2003, MS from the Institute of Pattern Recognition, Shanghai Jiaotong University, in 2006, and his PhD from the Department of Computer and Information Sciences, University of Delaware, in 2011. He joined Mitsubishi Electric Research Labs as a visiting research scientist in November 2011. His research interests include multi-camera system design and applications, fluid surface reconstruction and medical imaging. He is a member of the IEEE.

Jie Yang received his PhD in computer science from the University of Hamburg, Germany. He is now a professor and director of the Institute of Image Processing and Pattern Recognition, Shanghai Jiao Tong University. He has led more than 30 national and ministry scientific research projects in image processing, pattern recognition, data amalgamation, data mining, and artificial intelligence.

Jingyi Yu is an Associate Professor in the Department of Computer & Information Sciences and the Department of Electrical & Computer Engineering at the University of Delaware. He received his B.S. from Caltech in 2000 and Ph.D. from MIT in 2005. His research interests span a range of topics in computer vision and computer graphics, especially on computational cameras and displays. He has served as a Program Chair of OMNIVIS 11, a General Chair of Projector-Camera Systems 08, and an Area and Session Chair of ICCV 11. He is a recipient of both the NSF CAREER Award and the AFOSR YIP Award.

Yasuyuki Matsushita received his B.S., M.S. and Ph.D. degrees in EECS from the University of Tokyo in 1998, 2000, and 2003, respectively. He joined Microsoft Research Asia in April 2003. He is a Lead Researcher in Visual Computing Group. His areas of research are photometric methods in computer vision. He is on the editorial board member of IEEE Transactions on Pattern Analysis and Machine Intelligence (TPAMI), International Journal of Computer Vision (IJCV), IPSJ Journal of Computer Vision and Applications (CVA), The Visual Computer Journal, and Encyclopedia of Computer Vision. He served/is serving as a Program Co-Chair of PSIVT 2010, 3DIMPVT 2011, and ACCV 2012. He is appointed as a Guest Associate Professor at Osaka University (April 2010-), Visiting Associate Professor at National Institute of Informatics (April 2011-) and Tohoku University (April 2012-), Japan. He is a senior member of IEEE.

Michael S. Brown obtained his BS and PhD in Computer Science from the University of Kentucky in 1995 and 2001 respectively. He is currently an Associate Professor and Assistant Dean (External Relations) in the School of Computing at the National University of Singapore. Dr. Browns research interests include computer vision, image processing and computer graphics. He has served as an area chair for CVPR, ICCV, ECCV, and ACCV and is currently an associate editor for the IEEE Transactions on Pattern Analysis and Machine Intelligence (TPAMI).